Article

SOURCE DATA | TRANSPARENT PROCESS

THE EMBO JOURNAL

Placing steroid hormones within the human ABCC3 transporter reveals a compatible amphiphilic substrate-binding pocket

Jie Wang[1,2], Xu Li[1,2], Fang-Fang Wang[1,2], Meng-Ting Cheng[1,2], Yao-Xu Mao[1,2], Shu-Cheng Fang[1,2], Liang Wang[2], Cong-Zhao Zhou[1,2,*], Wen-Tao Hou[1,2,**] & Yuxing Chen[1,2,***]

Abstract

The human ABC transporter ABCC3 (also known as MRP3) transports a wide spectrum of substrates, including endogenous metabolites and exogenous drugs. Accordingly, it participates in multiple physiological processes and is involved in diverse human diseases such as intrahepatic cholestasis of pregnancy, which is caused by the intracellular accumulation of bile acids and estrogens. Here, we report three cryogenic electron microscopy structures of ABCC3: in the apo-form and in complexed forms bound to either the conjugated sex hormones β-estradiol 17-(β-D-glucuronide) and dehydroepiandrosterone sulfate. For both hormones, the steroid nuclei that superimpose against each other occupy the hydrophobic center of the transport cavity, whereas the two conjugation groups are separated and fixed by the hydrophilic patches in two transmembrane domains. Structural analysis combined with site-directed mutagenesis and ATPase activity assays revealed that ABCC3 possesses an amphiphilic substrate-binding pocket able to hold either conjugated hormone in an asymmetric pattern. These data build on consensus features of the substrate-binding pocket of MRPs and provide a structural platform for the rational design of inhibitors.

Keywords ABCC3; cryo-EM; hormone; multidrug resistance; substrate-binding pattern

Subject Category Structural Biology

DOI 10.15252/embj.2022113415 | Received 31 December 2022 | Revised 15 June 2023 | Accepted 20 June 2023

The EMBO Journal (2023) e113415

Introduction

The human ABCC family contains 12 members, ABCC1–ABCC12, all of which are type IV ABC transporters (Thomas & Tampé, 2020). The family can be further divided into three smaller functional groups: multidrug resistance proteins (MRPs, ABCC1-6 and ABCC10-12), the cystic fibrosis transmembrane conductance regulator (CFTR, ABCC7), and sulfonylurea receptors (SUR, ABCC8 and ABCC9; Gu & Manautou, 2010). To date, only the structure and function of ABCC7 (Liu *et al*, 2017; Fiedorczuk & Chen, 2022a,b), ABCC8 (Lee *et al*, 2017; Wu *et al*, 2018; Martin *et al*, 2019), and ABCC9 (Sung *et al*, 2021) have been thoroughly studied.

Drug resistance in cancer patients mediated by ABC transporters is a key factor of chemotherapy failure in the clinic. In this respect, both ABCB (also termed MDR) and ABCC families, in addition to ABCG2 from the ABCG family, are prominent (Gottesman *et al*, 2002). Elucidation of the multidrug-resistant mechanism of ABCB1 (Aller *et al*, 2009) has successfully guided the development of clinical inhibitors, such as elacridar (Dash *et al*, 2017). Despite structures of ABCC1 from cattle (bABCC1) (Johnson & Chen, 2017, 2018; Wang *et al*, 2020) and yeast (Bickers *et al*, 2021; Khandelwal *et al*, 2022) being reported, no structural information on human MRPs is available, hindering the development of effective drug efflux inhibitors for cancer treatment.

ABCC3 is widely expressed in various tissues such as the adrenal gland, liver, pancreas, gallbladder, and small intestine (König *et al*, 1999; Kool *et al*, 1999) and possesses a broad spectrum of substrate specificity (Kool *et al*, 1997). ABCC3 has been found to mediate drug transport across blood–tissue barriers, thus regulating drug delivery and pharmacokinetics (Kool *et al*, 1999; Ghanem & Manautou, 2019). In addition to exogenous drugs, ABCC3 is able to transport various endogenous metabolites, such as bilirubin glucuronides (Keppler, 2014), bile acids (Zeng *et al*, 2000), and steroid hormones (Lee *et al*, 2004). For instance, ABCC3 was found to transport conjugated hormones (Li *et al*, 2019; Järvinen *et al*, 2020), such as androgen dehydroepiandrosterone sulfate (DHEAS) and estrogen β-estradiol 17-(β-D-glucuronide) ($E_2$17βG) (Lee *et al*, 2004). DHEA is the most abundant steroid hormone in human plasma and serves

1 Department of Endocrinology, Institute of Endocrine and Metabolic Diseases, The First Affiliated Hospital of USTC, and Center for Advanced Interdisciplinary Science and Biomedicine of IHM, Division of Life Sciences and Medicine, University of Science and Technology of China, Hefei, China
2 Biomedical Sciences and Health Laboratory of Anhui Province, University of Science and Technology of China, Hefei, China
*Corresponding author. Tel: +86 55163602491; E-mail: cyxing@ustc.edu.cn
**Corresponding author. Tel: +86 55163602491; E-mail: todvince@mail.ustc.edu.cn
***Corresponding author. Tel: +86 55163602491; E-mail: zcz@ustc.edu.cn

as the precursor for a range of sex hormones, such as androstenedione, testosterone, estrone, and estradiol (Rutkowski *et al*, 2014), the primary estrogen for the maturation of sex organs (Stillwell, 2016). ABCC3 participates in maintaining the homeostasis of human steroid hormones by both circulating DHEAS (Appendix Fig S1A) among different tissues and excreting $E_2$17βG (Appendix Fig S1A) from the liver into hepatic blood sinusoids (Järvinen *et al*, 2020).

As a compensatory protein, ABCC3 is induced in the cholestatic state and exports bile acids out of hepatocytes to alleviate damage to the liver (Keppler & König, 2000; Keppler, 2014). Excess bile acids that accumulate in the liver are highly toxic to cells and cause diseases such as progressive familial intrahepatic cholestasis (PFIC) and intrahepatic cholestasis of pregnancy (ICP). Notably, ICP is a disorder of the liver usually observed in mid- and late-pregnancy that leads to perinatal asphyxia and, in some severe cases, newborn death (Gabzdyl & Schlaeger, 2015; Ovadia & Williamson, 2016). ICP is currently thought to be associated with elevated levels of estrogens such as estradiol (Gabzdyl & Schlaeger, 2015; Zu *et al*, 2021). Normally, excess estradiol is transported by ABCC2 to the bile duct in its conjugated form of $E_2$17βG (Morikawa *et al*, 2000). This transport inhibits the function of the bile salt export pump ABCB11 in a dose-dependent manner (Stieger *et al*, 2000), leading to cholestasis (Lammert *et al*, 2000). Intrahepatic cholestasis increases the amount of cellular ABCC3, relieving clinical symptoms, with ABCC3 excreting $E_2$17βG to the hepatic blood sinusoid, decreasing its concentration in the bile duct. In a separate function, ABCC3 can also directly mediate the efflux of accumulated bile acids from hepatocytes (Scheffer *et al*, 2002; Borst *et al*, 2007; Keppler, 2014).

Here, we report the apo-form structure of ABCC3 at 3.07 Å resolution and two substrate-bound structures of ABCC3 complexed with $E_2$17βG and DHEAS at 3.65 and 3.52 Å resolution, respectively. Structural analysis combined with biochemical assays revealed a V-shaped substrate-binding pocket accommodating two molecules of substrate in an asymmetric manner. Combined with previous reports, our findings provide structural insights into the wider substrate specificity of MRPs toward this group of conjugated hormone molecules. Moreover, these structures enable us to discover common features of the diverse substrates of MRPs and enhance our knowledge of multidrug resistance.

Results

Biochemical characterization and structure determination of ABCC3

Full-length human ABCC3, which is composed of 1,527 amino acid residues, was recombinantly overexpressed in human embryonic kidney (HEK) 293F cells and purified with detergent micelles of lauryl maltose neopentyl glycol (LMNG) and cholesteryl hemisuccinate (CHS). To better mimic the physiological membrane environment, we reconstituted detergent-solubilized ABCC3 in porcine brain polar lipid (BPL) nanodiscs utilizing the membrane scaffold protein MSP1D1 (Appendix Fig S1B and C). The purified ABCC3 in nanodiscs appeared to be stable and homogeneous, as confirmed by size-exclusion chromatography (Appendix Fig S1B), and possessed an ATPase activity in the absence of substrate with K_m and V_{max} values of 0.13 mM and 11.29 mol Pi min^{-1} mol^{-1} protein, respectively (Fig 1A). Upon the addition of $E_2$17βG, ABCC3 in nanodiscs showed a stimulated ATPase activity, with a half maximum effective concentration (EC_{50}) of 13.34 μM and a V_{max} of 31.93 mol Pi min^{-1} mol^{-1} protein (Fig 1B). Compared to that of $E_2$17βG, the addition of DHEAS yielded a comparable V_{max} of 32.75 mol Pi min^{-1} mol^{-1} protein and a significantly higher EC_{50} of 61.91 μM. Notably, the E1451Q mutation at the consensus site of ABCC3 that abolishes its ATPase activity (Fig 1A) showed no substrate-simulated ATPase activity upon the addition of either substrate (Fig 1B). These results indicated that our ABCC3 samples are in the physiologically relevant state and showed detectable discrepancy toward various substrates.

To gain structural insights into ABCC3 and further decipher the underlying translocation mechanism, we optimized these samples for single-particle cryogenic electron microscopy (cryo-EM) and eventually solved three structures of ABCC3: the apo-form, $E_2$17βG- and DHEAS-bound forms at 3.07, 3.65, and 3.52 Å, respectively (Appendix Fig S1D).

Overall structure of the apo-form ABCC3

The apo-form ABCC3 structure was solved at an overall resolution of 3.07 Å, and the resolution at the transmembrane regions is up to 2.50 Å (Appendix Fig S1D). The final model of apo-form ABCC3 was refined against the EM density to obtain excellent geometry and statistics that covers 1,364 residues (Appendix Table S1), with the exception of two flexible linkers (residues Ala268-Arg295, Cys850-Ala950) and two loops of residues Met1-Cys31 and Gly1525-Ala1527 (Appendix Fig S1E). ABCC3 possesses a canonical structure of full ABC transporter, which consists of two transmembrane domains (TMDs) and two nucleotide-binding domains (NBDs) (Rees *et al*, 2009). The TMDs harbor a vestibule containing substrate-binding sites in the membrane that participate in substrate recognition and transport; whereas the two NBDs possess a consensus and a degenerated ATP hydrolysis site, respectively. In addition, ABCC3 has an extra TMD consisting of five transmembrane helices (TMs) at the most N terminus, named TMD0 (Fig 1C).

Both TMD1 and TMD2 of ABCC3 possess six TMs with a significant cytosolic extension from the membrane that interact with the corresponding NBD via two coupling helices, which couple the conformational changes between TMDs and NBDs. TM9 and TM10 from TMD1, in addition to TM15 and TM16 from TMD2, are swapped to the opposite TMD, exhibiting a typical feature of type-IV transporter (Thomas & Tampé, 2020). The densities are relatively poor for the N-terminal TMD0 at a resolution of ~ 4 Å, which has also been observed in some members of ABCB and ABCC families (Thomas & Tampé, 2020). The function of TMD0 remains a paucity of evidence despite a couple of available clues from SUR (Chan *et al*, 2003), TAP (ABCB2/3) (Koch *et al*, 2004) and TAPL (ABCB9) (Demirel *et al*, 2010). For example, the SUR1 (ABCC8) structure indicates that TMD0 provides an interactive interface for the Kir6.2 tetramer, which forms a central potassium ion channel (Lee *et al*, 2017). The five helices of TMD0 of ABCC3 are tightly packed against each other, forming a compact and independent domain that is aligned against TMD1 via direct interactions between TM2 and TM6 (Fig 1D). The interactions between TMD0 and TMD1 are further stabilized by the lasso motif (residues Pro204-Ala272), which is partially inserted into the membrane and packed against TM15 and

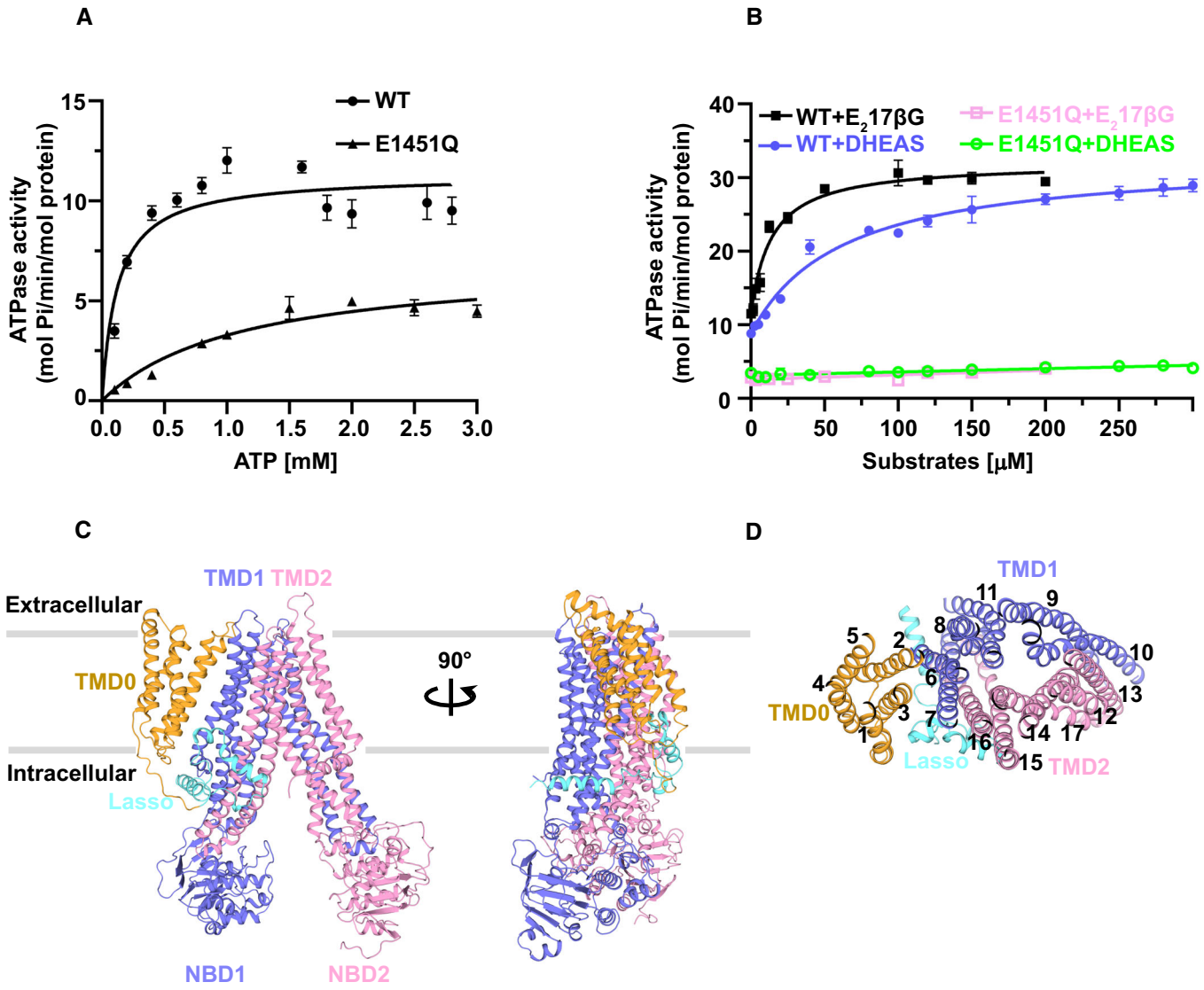

Figure 1. Substrate-stimulated ATPase activity assays and the overall structure of the apo-form ABCC3.

A ATPase activity of ABCC3 wild-type (WT) and E1451Q in nanodiscs. The data points for WT and E1451Q are fitted with a Michaelis–Menten equation.

B Substrate-stimulated ATPase activities of ABCC3 WT and E1451Q upon addition of substrate $E_2$17βG or DHEAS. All data points for (A) and (B) are the average of three independent experiments in nanodiscs, and error bars represent standard deviation.

C Cartoon representation of the apo-form ABCC3. TMD1 and NBD1 are colored in slate. TMD2 and NBD2 are colored in pink. TMD0 and lasso motif are colored in khaki and aquamarine, respectively. The membrane plane is indicated as the gray rectangle.

D Top view of the apo-form ABCC3. The 17 transmembrane helices (TMs) are sequentially numbered.

Source data are available online for this figure.

TM16 (Fig 1C and D). This C-family-featured lasso motif was demonstrated to be essential for the folding and full function of ABCCs (Bakos *et al*, 1998; Westlake *et al*, 2003).

ABCC3 shares a 58% sequence identity with ABCC1 (Kool *et al*, 1999) and possesses a couple of same substrates; however, ABCC3 has less reported substrates involved in multidrug resistance, compared to the well-investigated ABCC1 (Zeng *et al*, 1999; Borst *et al*, 2007). Structural comparison against bABCC1 gives a root-mean-square deviation (RMSD) of 1.664 Å over 1,126 Cα atoms, indicating that they have a similar overall structure.

Of note, TMD0 of ABCC3 shows a rigid body shift toward the core structure of TMD1 and TMD2 (Appendix Fig S1F), thus adopting a distinct pose compared to that of bABCC1 (Johnson & Chen, 2017), Ycf1 (Bickers *et al*, 2021), and SUR1 (Martin *et al*, 2019). TMD0 interacts with TMD1 via an interface of ~ 1,700 Å^2 mainly contributed by TM2 from TMD0 and TM6 from TMD1. In order to reveal the function of TMD0, we performed the ATPase activity assays of TMD0-truncated ABCC3, which showed a similar V_{max} at 13.01 mol Pi min^{-1} mol^{-1} protein and a higher K_m of 0.53 mM compared to the wild type (Appendix Fig S1G). We further

compared the substrate-stimulated ATPase activities and found no significant change upon the truncation of TMD0 (Appendix Fig S1H). Moreover, the vesicle-based transport activity assays using radioactive $E_2$17βG also displayed an activity comparable to that of full-length ABCC3 (Appendix Fig S1I). Notably, deletion of TMD0 does not alter the thermal stability of ABCC3 (Appendix Fig S1J). These results implicate that TMD0 is not involved in the transport activity of ABCC3; and more in-depth investigations are needed to decipher the bona fide function of TMD0.

Two $E_2$17βG molecules bind to ABCC3 in an asymmetric manner

In the complex structure of $E_2$17βG-bound ABCC3, two $E_2$17βG molecules could be perfectly fitted to the densities, which are asymmetrically located in the transmembrane cavity at a pose of inverted "V" (Fig 2A). Superposition with the apo-form structure reveals an RMSD of 2.350 Å over 1,313 Cα atoms. This indicates little conformational changes upon substrate binding, especially for the TMs, but side-chain rotations of some key residues in the binding pocket (Appendix Fig S2A). Both molecules are deeply buried in an inner membrane leaflet vestibule between TMD1 and TMD2. The hydrophobic cyclopentanoper-hydrophenanthrene skeleton (or the steroid nucleus) of the two $E_2$17βG molecules pack against each other, forming the arc of the inverted "V"; whereas the two conjugated glucuronides are separated and fixed by two hydrophilic patches in TMD1 and TMD2, respectively. The $E_2$17βG on TMD1 side ($E_2$17βG-1) is embraced by TM7, TM8, TM11, TM16, and TM17, with the glucuronide forming a salt bridge with R1193 from TM16 and two salt bridges with R1245 from TM17, respectively (Fig 2B). In addition, Y371 and F375 from TM7, L429 from TM8 and M548 from TM11 support a hydrophobic environment for the steroid nucleus. The $E_2$17βG molecule on TMD2 side ($E_2$17βG-2) is surrounded by TM10, TM11, and TM17, without polar interactions that fix the glucuronide. In addition, we could find a hydrogen bond between the 3′ hydroxyl group of the steroid nucleus and N1241 from TM17. $E_2$17βG-2 is mostly fixed by nonpolar interactions, including W539 from TM10, M584 from TM11, F1238 and W1242 from TM17, in addition to hydrophobic stacking against $E_2$17βG-1.

Site-directed mutagenesis combined with ATPase activity assays indicated that the ABCC3 variants with a single mutation of $E_2$17βG-binding residues, either those forming polar interactions with the glucuronide portion (R1193A/K/Q, R1245A/K/Q and N1241A) or hydrophobic interactions with the steroid nucleus (Y371A, F375A, L429A, W539A, F1238A, and W1242A), displayed a significant decrease in substrate-simulated ATPase activity, compared to that of the wild type (Fig 2C; Appendix Fig S2B). Of note, unlike W1242A, W1242F/Y showed a comparable activity with the wild type, indicating that various aromatic stacking could also support $E_2$17βG binding. On the other hand, all kinds of substitutions of the two arginine residues (R1193 and R1245) could lead to a completely abolished substrate-stimulated ATPase activity, indicating that a long side chain of arginine is necessary. The results well explained why these two arginine residues (R1193 and R1245) are highly conserved among ABCC3 homologs (Appendix Fig S2C). We also performed vesicle-based transport activity assays using radioactive $E_2$17βG, as well as binding assays using surface plasmon resonance (SPR). Most variants showed decreased transport activities compared to the wild type, except for L429A, N1241A, and W1242A (Fig 2D). In fact, L429 forms rather weak hydrophobic interactions with $E_2$17βG-1, while N1241 and W1242 contribute to $E_2$17βG-2 binding (Fig 2B). In addition, the results of the binding assays are consistent with those of the substrate-stimulated ATPase activity assays: all variants showed decreased affinity toward $E_2$17βG, especially R1193A and R1245A, which displayed a very sharp decrease (Fig 2E; Appendix Fig S3). Altogether, we concluded that polar interactions play a major role in substrate binding, and the residues binding to $E_2$17βG-1 are more determinant, which is consistent with the observation of the rather poor electron density of glucuronide in $E_2$17βG-2 compared to that in $E_2$17βG-1 (Appendix Fig S4). Sequence alignment revealed that all these residues, except for Y371, are conserved among ABCC3 homologs (Appendix Fig S2C). Moreover, most polar residues contributing to the hydrogen bonds or salt bridges, namely N1241, R1193, and R1245, are also highly conserved among MRPs (Appendix Fig S5).

The hydrophilic conjugation group determines the orientation of DHEAS binding to ABCC3

Despite sharing a similar steroid nucleus, $E_2$17βG has a conjugation of glucuronide at the 17′ hydroxyl group, whereas DHEAS has a different polar group, a sulfate group, conjugated to the 3′ hydroxyl group of the steroid nucleus (Appendix Fig S1A). Therefore, we solved the DHEAS-bound ABCC3 structure in nanodiscs at 3.52 Å resolution. In the structure, we observed two extra densities, which fit two DHEAS molecules perfectly, at the same pocket in the $E_2$17βG-complexed structure (Fig 3A; Appendix Fig S6A).

Figure 2. Overall structure of $E_2$17βG-bound ABCC3 and the substrate-binding pocket.

A Side and top views of the overall structure of $E_2$17βG-bound ABCC3. TMD1 and NBD1 are colored in slate. TMD2 and NBD2 are colored in pink. TMD0 and lasso motif are colored in khaki and aquamarine, respectively. The membrane plane is indicated as the gray rectangle. Density maps of $E_2$17βG, shown as gray mesh, are contoured at 3 σ. Two $E_2$17βG molecules are shown as green/red spheres. The TMs are numbered in the top view.

B The binding pocket of $E_2$17βG. The interacting residues are shown as sticks and colored in slate (from TMD1) or pink (from TMD2). The hydrogen bonds and salt bridge are indicated by blue and black dotted lines, respectively. Interacting residues of each E217βG molecule are shown by two zoom-in images, respectively. Two $E_2$17βG molecules are shown as sticks.

C Relative ATPase activities of ABCC3 WT and mutants in the presence of 2 mM ATP upon addition of $E_2$17βG. The relative activity represents the substrate-stimulated activity of ABCC3 WT or its mutants harboring mutation of residues at the substrate-binding pocket.

D Transport [^{3}H]-$E_2$17βG activity assays of ABCC3 WT and mutants. For (C) and (D), the activities of ABCC3 WT are set as 100%. One-way analysis of variance (ANOVA) is used for the comparison of statistical significance of mutants and WT. The *P* values of < 0.05, 0.01, and 0.001 are indicated with *, ** and ***, respectively.

E Affinity of ABCC3 WT and mutants for $E_2$17βG detected by surface plasmon resonance (SPR).

Source data are available online for this figure.

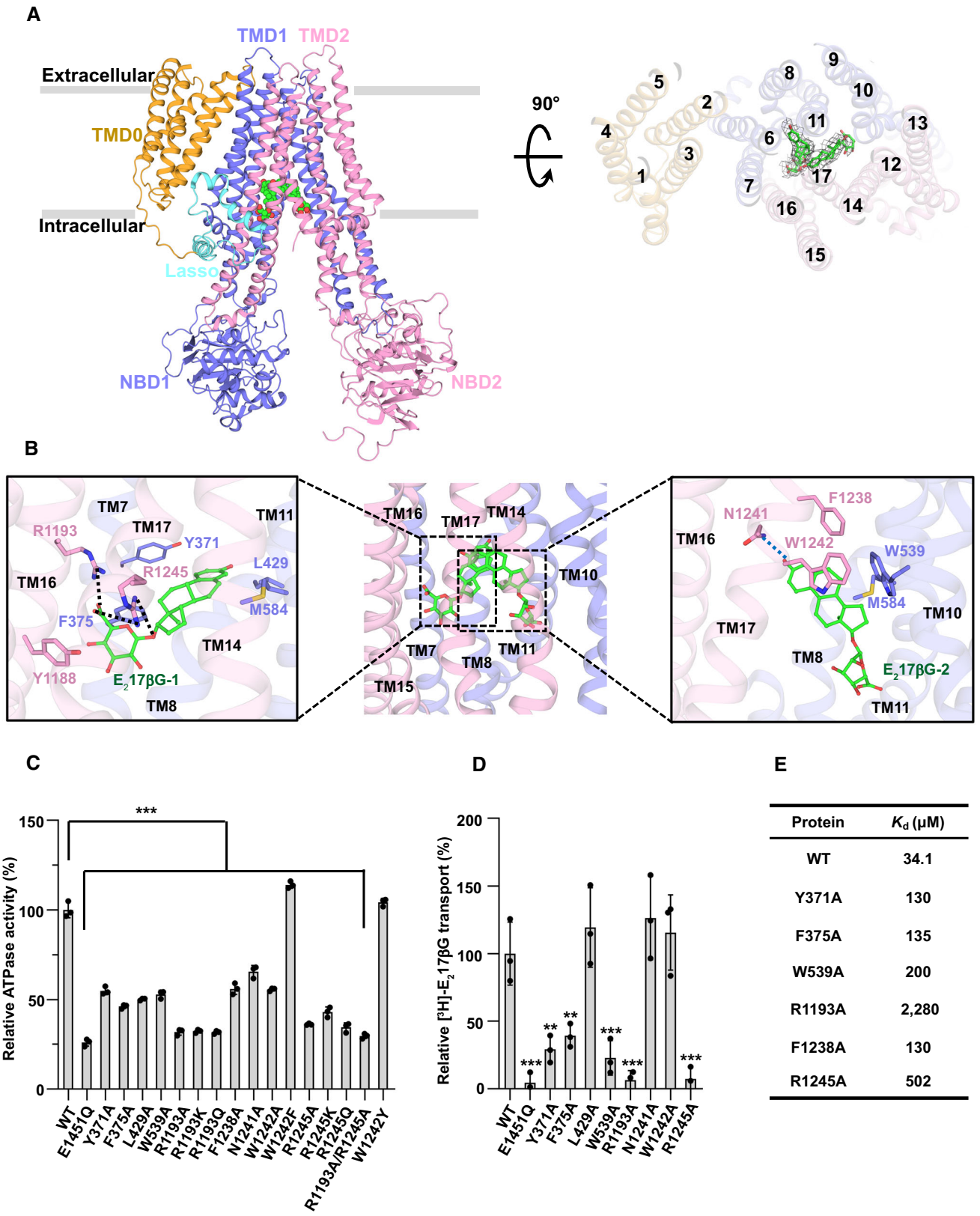

E

Protein	K_d (μM)
WT	34.1
Y371A	130
F375A	135
W539A	200
R1193A	2,280
F1238A	130
R1245A	502

Figure 2.

Superposition with the $E_2$17βG-bound structure revealed an RMSD of 0.837 Å over 1,136 Cα, indicating quite a resemblance between the two complex structures. However, despite sharing a similar V-shaped binding pattern, the two DHEAS molecules display a reversed orientation of the steroid nucleus compared to that of $E_2$17βG (Appendix Fig S6B).

In this structure, the sulfate group of DHEAS on TMD1 side (DHEAS-1) forms a salt bridge with R1193 from TM13 and R1245 from TM17, respectively (Fig 3B). On the other hand, the unconjugated 17′ carbonyl group of DHEAS-1 is stabilized via a hydrogen bond with K318 from TM16. Concerning the DHEAS molecule on TMD2 side (DHEAS-2), the sulfate group forms a hydrogen bond with T535 from TM10. Notably, N1241 from TM17, which forms a hydrogen bond with $E_2$17βG-2, does not contribute to the interaction with DHEAS-2. Similar to those in the $E_2$17βG-bound structure, a cluster of hydrophobic residues, namely Y371, F375, P425, F426, L429, W539, L580, M584, F1238, and W1242, stabilizes the two DHEAS molecules that pack against each other via the steroid nucleus (Appendix Fig S6C). Subsequent site-directed mutagenesis combined with activity assays revealed a significant decrease in DHEAS-stimulated ATPase activity resulting from the individual single mutations of DHEAS-interacting residues, compared to the wild-type ABCC3 (Fig 3C; Appendix Fig S2B). We further performed DHEAS-binding assays of the variants using SPR, which all showed decreased affinities (Fig 3D; Appendix Fig S7). Notably, single mutation of the hydrophilic residues R1245, R1193, and K318 to Ala led to a sharp decrease in affinity toward DHEAS. In addition, mutations of the binding residues shared by DHEAS and $E_2$17βG display a similar profile in both assays. However, as ABCC3 has a higher binding affinity toward $E_2$17βG, the corresponding mutants possess a sharper decrease in substrate-stimulated ATPase activity, compared to that of DHEAS (Figs 2C and 3C).

Compared to the corresponding $E_2$17βG molecule, DHEAS-1 is slightly uplifted toward the outer membrane leaflet, whereas the steroid nucleus of DHEAS-2 and $E_2$17βG-2 could be largely superimposed (Appendix Fig S6B). The variance is most likely due to the different chemical structures of DHEAS-2 and $E_2$17βG-2, which possess a conjugation group at the opposite ends of the steroid nucleus, respectively (Appendix Fig S1A). Of note, DHEAS is stabilized by more residues, namely the polar residue K318 and T535, which forms hydrogen bonds, and P425, F426, L580 and M1089, which contribute to hydrophobic interactions. Sequence alignment revealed that these residues are also conserved among ABCC3 homologs (Appendix Fig S2C). As predicted, the K318A and T535A variants possessed a decreased $E_2$17βG-stimulated ATPase activity compared to the wild type (Fig 3E). In particular, the single mutation of K318A resulted in a decreased affinity toward $E_2$17βG (Appendix Fig S3).

In conclusion, the substrate-binding pockets accommodating DHEAS and $E_2$17βG share a common feature: a large hydrophobic surface and two small polar patches, which are complementary to the steroid nucleus and the conjugation group of various substrates, respectively. Combined with the results of biochemical assays, it revealed that the polar patch on TMD1 plays a more important role in substrate binding and transport.

Discussion

The detoxification of endogenous and exogenous toxins to human beings, which are usually hydrophobic compounds, is generally driven by enzymes in the liver via conjugation with various polar groups (Grant, 1991). Glucuronide is one of the most common polar groups that is produced through glycometabolism and conjugated to the hydroxyl, carboxyl, amino, or other groups of toxins by UDP-glucosyltransferases in the human liver (Tukey & Strassburg, 2000; Yang *et al*, 2017). In addition, other types of polar groups, such as glutathione, sulfate, and acetyl groups, could also be conjugated to various toxins (Kulsharova & Kurmangaliyeva, 2021). Eventually, these conjugated toxins are pumped out by various MRPs to the excretory system (Yang *et al*, 2017).

As ABCC3 can excrete both $E_2$17βG and bile acids from the liver (Borst *et al*, 2007), it might become a promising target for ICP therapy (Rao *et al*, 2017). In addition, patients with ICP usually suffer from jaundice (Wilson & Haverkamp, 1979), a disease caused by the intrahepatic accumulation of bilirubin, which could also be excreted by ABCC3 (Lee *et al*, 2004). Therefore, the structure-based design of ABCC3 agonists may be a promising strategy for the drug development for ICP therapy. In fact, a combined administration of three drugs targeting ABCC7 has been applied to the treatment of cystic fibrosis (Middleton *et al*, 2019). Recently, a couple of drug-bound ABCC7 structures also provide more insights for the rational optimization of these clinical drugs (Fiedorczuk & Chen, 2022a,b; Levring *et al*, 2023).

After analysis of the previously reported substrates of MRPs, we found that they all share a common feature: a negatively charged group conjugated to a hydrophobic core structure (Appendix

Figure 3. Overall structure of DHEAS-bound ABCC3 and the substrate-binding pocket.

A Side and top view of the overall structure of DHEAS-bound ABCC3. TMD1 and NBD1 are colored in slate. TMD2 and NBD2 are colored in pink. TMD0 and lasso motif are colored in khaki and aquamarine, respectively. The membrane plane is indicated as the gray rectangle. Density maps of DHEAS, shown as gray mesh, are contoured at 4 σ. Two DHEAS molecules are shown as orange spheres or sticks. The TMs are numbered in the top view.

B The binding pocket of DHEAS. The interacting residues are shown as sticks and colored in slate (from TMD1) or pink (from TMD2). The hydrogen bonds and salt bridges are indicated by blue and black dotted lines, respectively. Interacting residues of each DHEAS molecule are showed by two zoom-in images, respectively.

C Relative ATPase activities of ABCC3 WT and mutants in nanodiscs upon addition of DHEAS and 2 mM ATP. The relative activity represents the substrate-stimulated activity of ABCC3 WT or mutants harboring mutation of residues at the substrate-binding pocket.

D Affinity of ABCC3 WT and mutants for DHEAS detected by SPR.

E Relative ATPase activities of ABCC3 WT and mutants K318A, T535A upon addition of $E_2$17βG. For (C) and (E), the activities of ABCC3 WT are set as 100%. One-way ANOVA is used for the comparison of statistical significance of mutants and WT. The *P* values of < 0.05, 0.01, and 0.001 are indicated with *, ** and ***, respectively.

Source data are available online for this figure.

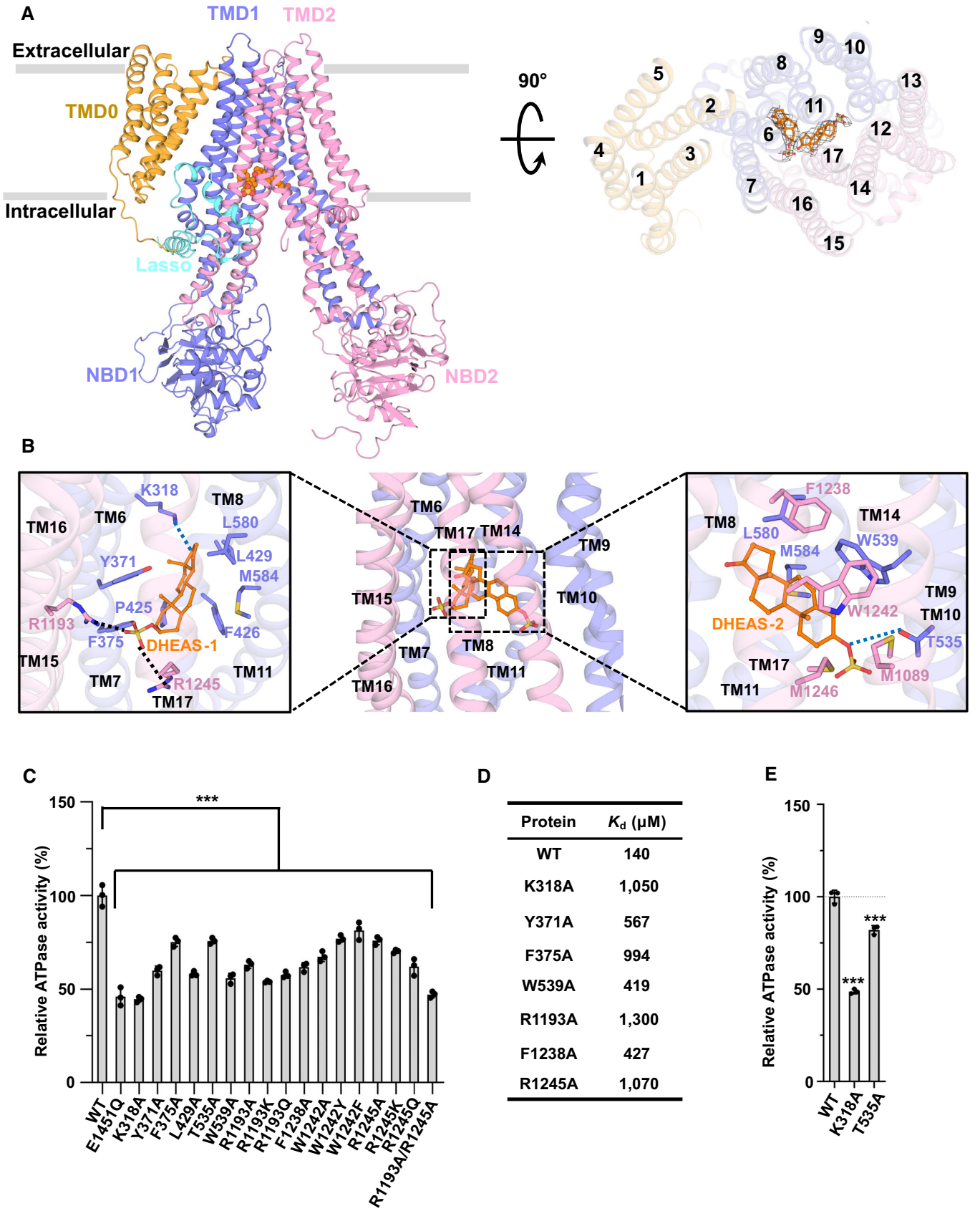

Figure 3.

Table S2). Consistently, as shown in our ABCC3 structures, the substrate-binding pocket possesses a hydrophobic cavity in addition to two hydrophilic patches (Fig 4A). However, the sequence alignment showed that a cluster of positively charged residues in the substrate-binding pocket of TMD1 side is highly conserved; whereas the residues of the other polar patch at the TMD2 side are rather variable (Fig 4B; Appendix Fig S8). According to the size and conjugation type, we classify all identified substrates of MRPs into three

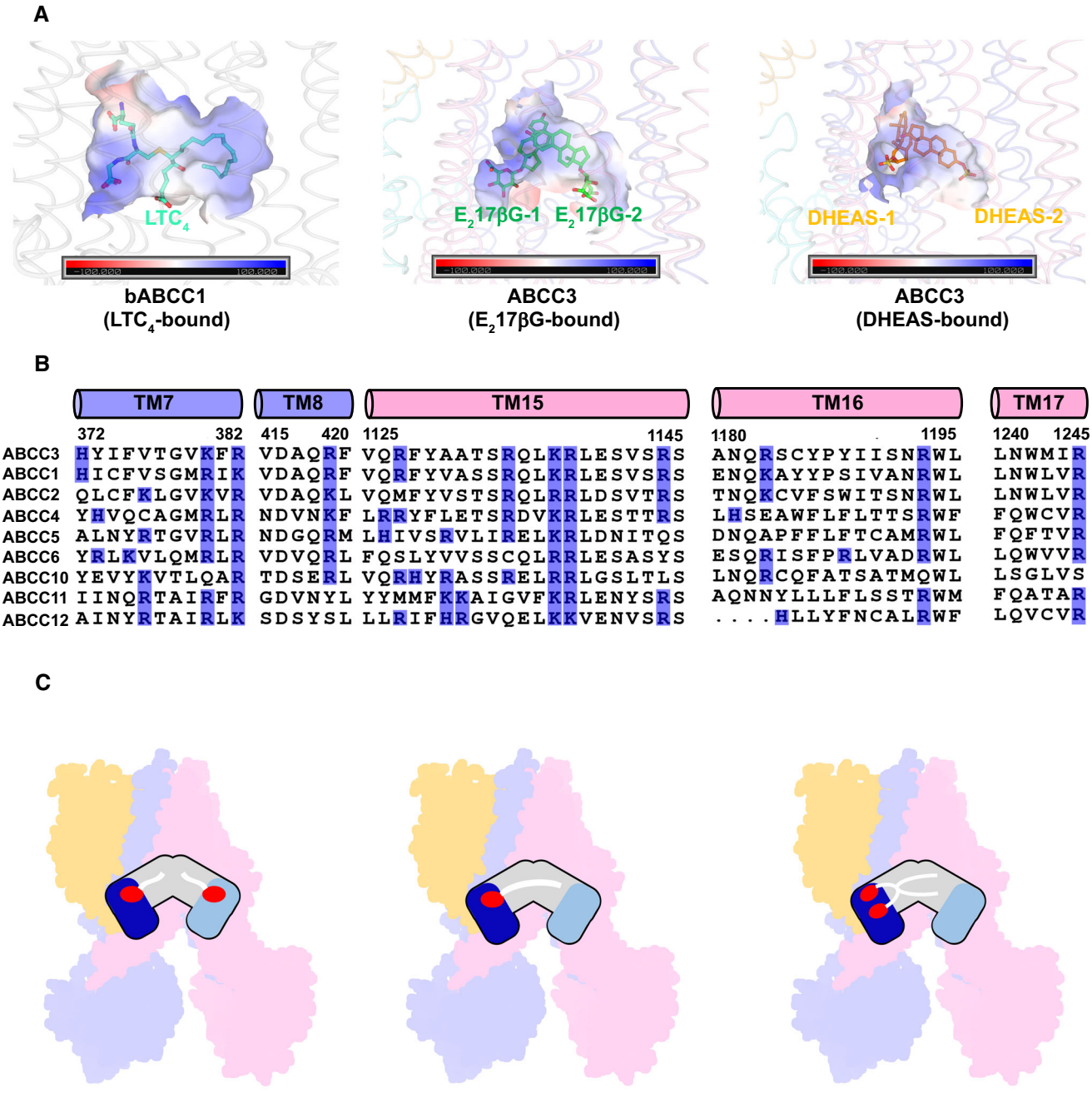

Figure 4. Proposed substrate-binding patterns of MRPs.

A The electrostatic potential of substrate binding pocket in bABCC1 (PDB 5UJA) or ABCC3. Scale: red, negative (−100 Kt/e); blue, positive (+100 Kt/e).

B Multiple-sequence alignment of the substrate binding residues of MRPs. TMs are shown as columns in slate for TMD1 and pink for TMD2. Positively charged residues that bind to the negatively charged group of substrates are colored in blue.

C Three putative substrate-binding patterns of MRPs. The conserved positively charged patch in TMD1 is colored in dark blue, and the less conserved positively charged patch in TMD2 is colored in light blue. The negatively charged conjugation group of the substrate is represented by a red oval, and the hydrophobic core is represented by a white ribbon.

groups: small substrates of single conjugation and large substrates of single or double conjugation.

Based on the present structures and previous reports (Appendix Table S2), we propose three binding patterns of MRPs (Fig 4C). For the small substrate of single conjugation, two small conjugated molecules could simultaneously bind to the substrate-binding pocket, as shown in our case. It is noteworthy that the two substrates might bind in an asymmetric pattern, as the binding patch in TMD2 is relatively weaker in hydrophilicity. For the large substrate of single conjugation, only one molecule could be accommodated in the pocket, with its negatively charged conjugation group fixed by the polar patch of TMD1 side and hydrophobic core structure buried in the hydrophobic cavity. This binding pattern is supported by the complex structure of bABCC1 (Johnson & Chen, 2017), in which the negatively charged glutathione portion of leukotriene C4 (LTC4) is stabilized by the polar patch, and the arachidonic acid of LTC4 is fitted in the hydrophobic cavity (Fig 4A). It is known that LTC4 is also a substrate of ABCC3 (Zeng *et al*, 2000; Zehnpfennig *et al*, 2009); thus, we predict that ABCC3 should accommodate only one molecule of LTC4 in a pattern similar to that in bABCC1. For the large substrate of double conjugations, such as bilirubin diglucuronide in ABCC2 (Jedlitschky *et al*, 1997) or cyclic GMP-AMP in ABCC1 (Maltbaek *et al*, 2022), we hypothesize that the two negatively charged conjugation groups should be primarily accommodated at the positively charged binding pocket at TMD1 side, which is comparable to the substrate-binding pocket of ABCC3 in volume (Fig 4; Appendix Fig S8). Superposition of our substrate-bound ABCC3 structures onto the bABCC1 structure in the outward-facing conformation (PDB: 6BHU) suggested that shifts of TM10, TM11, TM16, and TM17 will lead to the collapse of the substrate-binding pocket in an outward-facing conformation of ABCC3 (Appendix Fig S9). Altogether, the common feature of endogenous metabolites and exogenous toxins/drugs enables MRPs to possess a wide spectrum of various substrates, also leading to the gain of function of the multidrug resistance beyond detoxification. In contrast, MDRs from ABCB family, which export mostly hydrophobic substrates, possess a substrate-binding pattern different from MRPs (Seelig *et al*, 2000; Sharom, 2011; Johnson & Chen, 2017).

In summary, our structures not only provide the mechanism of the substrate specificity of ABCC3 but also reveal a common substrate-binding pattern for all MRPs, which further broadens our understanding of multidrug resistance.

Materials and Methods

Protein expression and purification

The full-length human *ABCC3* gene (UniProt ID: O15438) was synthesized by Sangon Biotech Company after codon optimization by eukaryotic expression system. Wild-type *ABCC3* was subcloned into a pCAG vector with a C-terminal Flag-tag (DYKDDDDK) using a ClonExpress® II One Step Cloning Kit (Vazyme Biotech Co., Ltd). Using homologous recombination of multiple fragments, all point mutations were introduced by designing forward and reverse primers with point mutations and overlapped amplifying fragments. A truncated version of TMD0 (amino acids Asp2-Val202) was obtained by double-fragment-homologous recombination. For protein expression, HEK293 cells were cultured in SMM 293T-II medium (Sino Biological Inc.) at 37°C and 130 rpm with 5% CO_2. Cells were transfected when the density reached 2.5 ~ 3 × 10^6 cells per milliliter. For cell transfection, 1.8–2 mg plasmids were premixed with 4 mg linear polyethylenimines (PEIs) (Polysciences, Inc) of 25,000 MW in 45 ml fresh medium for 15 min, then the mixture was added to 800 ml HEK293F cells, supplemented with another 45 ml medium, and incubated once more for 15 min at rest. The transfected cells were grown at 37°C for 48–60 h before harvesting. Cell pellets were resuspended in the lysis buffer containing 50 mM Tris–HCl pH 8.0, 150 mM NaCl, 20% (v/v) glycerol, and ethylenediaminetetraacetic acid (EDTA)-free protease inhibitor cocktail (TargetMol) after centrifugation at 5,000 rpm for 7 min. The suspension was flash-frozen in liquid nitrogen and stored at −80°C for further use.

For protein purification, the thawed suspension was incubated in the lysis buffer with an additional 1% (w/v) LMNG (Anatrace) and 0.1% (w/v) CHS (Anatrace) with gentle rotation at 4°C for 2 h. Insoluble material was removed by ultracentrifugation at 45,000 rpm for 45 min (Beckman, Type 70 Ti) at 4°C. The supernatant was incubated in a decolorization shaker with the anti-FLAG M2 affinity gel (Sigma) on ice for 1 h. The resin was then loaded onto the column and washed five times, each time with 5 ml of wash buffer containing 50 mM Tris–HCl pH 8.0, 150 mM NaCl, 10% (v/v) glycerol, 0.005% (w/v) LMNG, and 0.0005% (w/v) CHS. Protein was eluted in batches to 6 ml after 15 min incubation with elution buffer containing 50 mM Tris–HCl pH 8.0, 150 mM NaCl, 5% (v/v) glycerol, 0.005% (w/v) LMNG, 0.0005% (w/v) CHS plus 200 μg/ml FLAG peptide. The eluate was then collected and concentrated using a 100-kDa MWCO Amicon Ultra centrifugal filter (Millipore) before being applied to size-exclusion chromatography by a Superose 6 Increase 10/300 gel filtration column (GE Healthcare) equilibrated in 50 mM Tris–HCl pH 8.0, 150 mM NaCl, 0.005% (w/v) LMNG, and 0.0005% (w/v) CHS. Peak fractions were pooled and flash-frozen in liquid nitrogen for future functional experiments or concentrated for nanodiscs reconstitution. All steps were performed either in cold storage or on ice.

Nanodiscs preparation

For nanodiscs preparation, concentrated ABCC3 was reconstituted into lipid nanodiscs by mixing with purified MSP1D1 scaffold protein (Ritchie *et al*, 2009) and porcine brain polar lipid extract (BPL, Avanti) at a 1:5:250 molar ratio. After 1 h of incubation on ice with shaking, 800 mg/ml Bio-beads SM-2 resin (Bio-Rad) was added to the mixture to initiate the nanodiscs reconstitution reaction by removing the detergent. The mixture was incubated overnight in cold storage with constant rotation. The bio-beads were removed, and the mixture was cleared of debris by centrifugation. The supernatant was loaded onto a Superose 6 Increase 10/300 GL column in 50 mM Tris–HCl pH 8.0 and 150 mM NaCl buffer without detergent. Peak fractions were collected and concentrated for EM analysis or biochemical studies.

ATPase activity assays

ATPase activities of wild-type ABCC3 and all mutants in the nanodiscs were measured using the ATPase colorimetric Assay Kit (Innova Biosciences) in 96-well plates at OD_{630nm} (Vardakou

et al, 2014). For the substrate-stimulated ATPase activity assay, a final concentration of 0.05 μM protein was added in the reaction buffer consisting of 25 mM Tris–HCl pH 8.0, 50 mM KCl, 2 mM $MgCl_2$, and 2 mM ATP (Sigma) to 80 μl as one reaction sample. Reactions were performed at 37°C for 1 h, and the amount of released phosphate group (Pi) was quantitatively measured using a SpectraMax iD5 Multi-Mode Microplate Reader (Molecular Devices). Estradiol 17-(β-D-glucuronide) sodium salt was purchased from GLPBIO, and dehydroepiandrosterone sulfate sodium salt was purchased from shyuanye. Both of them were dissolved in DMSO. The control groups in the absence of proteins were subtracted as background for each data point. Data are presented as the means ± SD by biological repeats from three independent assays (n = 3).

Membrane vesicle preparation

HEK 293F cells were collected at 4200 rpm for 10 min. Then, cell pellets were resuspended in 50 mM mannitol, 2 mM EGTA, 50 mM Tris–HCl pH 7.0 and homogenized by a Dounce tissue grinder (Sigma), supplemented with EDTA-free protease inhibitor cocktail. The unground cells and large organelle of grinding solution were removed by centrifugation at 3,000 *g* for 10 min. The supernatant was centrifuged at 100,000 *g* for 60 min. Then, the vesicles were resuspended in transport buffer consisting of 50 mM sucrose, 100 mM KNO3, 10 mM $Mg(NO_3)_2$, 10 mM Tris–HCl pH 7.4 and homogenized with a 0.45 mm needle to aid in vesicle formation. The resuspended vesicles were used for transport activity assays, immediately.

Transport activity assays

Transport activity assays were performed in membrane vesicles using the rapid filtration method. HEK293F cell membrane vesicles were incubated at 37°C in 50 mM sucrose, 100 mM KNO_3, 10 mM $Mg(NO_3)_2$, 10 mM Tris–HCl pH 7.4 and [^{3}H]-$E_2$17βG (PerkinElmer, Inc) in a final volume of 20 μl in the presence or absence of 2 mM ATP. After incubation for 60 s, the reaction was terminated by the addition of 80 μl ice-cold stop buffer consisting of 50 mM sucrose, 100 mM KNO_3, 10 mM Tris–HCl pH 7.4. After filtration by glass microfiber filters (GF/F, Whatman) with a nominal pore size of 0.7 μm, an additional 6 ml of stop buffer was used to eliminate excessive [^{3}H]-$E_2$17βG. The vesicle-associated radioactivity was determined by Tri-Carb 2910TR liquid scintillation counter (PerkinElmer, Inc). The amounts of proteins in the membrane vesicles for each preparation were quantified by purifying the proteins from the same batch of cells. Data are presented as the means ± SD by biological repeats from three independent assays (n = 3).

Microscale fluorescent thermal stability assay

CPM dye (Invitrogen) was dissolved in DMSO (Sigma) at 4 mg/ml. The dye stock was diluted 1:5 in buffer consisting of 50 mM Tris–HCl pH 8.0, 150 mM NaCl. The purified samples of WT and $ABCC3_{\Delta TMD0}$ in nanodiscs were diluted to a concentration of 1 μM. Then, 2 μl of the diluted dye was added to 18 μl protein samples and thoroughly mixed. The reaction mixture was heated in a controlled manner with a ramp rate of 6°C/min in a LightCycler 480 System (Roche). Assays were performed over a temperature range starting from 37°C and ending at 100°C.

Cryo-EM sample preparation and data collection

For the apo-form structure sample, the purified protein in nanodiscs was concentrated to ~ 1.4 mg/ml. An aliquot of 3.5 ml of the sample was applied to glow-discharged Quantifoil R1.2/1.3 300-mesh Cu Holey Carbon Grids. The grids were blotted for 5 s with a blot force −2, and then plunged into liquid ethane using a Vitrobot Mark IV (FEI) at 8°C and 100% humidity. Two datasets with a total of 3,023 micrograph stacks were automatically collected with EPU software on a Titan Krios microscope at 300 kV equipped with a K3 Summit direct electron detector (Gatan) and a GIF Quantum energy filter (Gatan) at the Center for Integrative Imaging, University of Science and Technology of China. All movie micrographs comprising 30 frames were collected in the super resolution mode at a nominal magnification of 81,000×, which yielded a pixel size of 0.535 Å. The first and second datasets were exposed under a total electron dose of 51 and 55 electrons $e^-/Å^2$, respectively, with a range from −2.2 to −1.5 μm of the defocus. For substrate bound structures, the purified ABCC3 in nanodiscs was concentrated to 1.85 mg/ml and incubated for 30 min with 1 mM $E_2$17βG or DHEAS in 5% (v/v) DMSO. With the addition of the $E_2$17βG sample, a total of 1,954 photographs comprising 32 frames were collected in a total electron dose of 54 electrons $e^-/Å^2$. The defocus was set at a range from −2.5 to −1.5 μm. For the cryo-EM data of the DHEAS-bound structure, two datasets with a total of 3,640 movie micrographs were collected in the same manner as the $E_2$17βG-bound ABCC3 structure. For all of these stacks, motion correction and dose weighting were performed with patch motion correction with a Fourier cropping factor of 0.535, resulting in a pixel size of 1.07. Meanwhile, the defocus values were estimated using Patch CTF estimation (Punjani *et al*, 2017).

Cryo-EM data processing

For the apo-form ABCC3 datasets, the first dataset of 802 micrographs picked out 126,993 particles by reference-based auto-pick, besides 640,062 particles were automatically picked from other 2,221 micrographs, using cryoSPARC v3.1.0 (Punjani *et al*, 2017), respectively (Appendix Fig S10A–E). After 2D classification, 126,993 particles with structural features were extracted from the first dataset, and 640,062 particles were extracted from the second one. The two sets of data are iterated ab initial and heterogeneous refinement, respectively, and the class particles with the better 3D model are selected. Then, we merged all the good particles together for homogeneous refinement as well as non-uniform refinement. Finally, a total of 587,916 particles were selected for local refinement with an adapted mask and yielded a reconstruction with an overall resolution of 3.07 Å.

For $E_2$17βG-bound ABCC3 datasets, 408,519 particles and 919,077 particles from two datasets were respectively picked and subjected to 2D classification and initial global search 3D classification after patch motion and patch CTF (Appendix Fig S11A–E). After several rounds of calculations, the structures were obtained after reconstruction with overall resolutions of 4.25 Å and 3.73 Å. Then, the corresponding 177,500 particles merged, were calibrated by homogeneous refinement and non-uniform refinement, and yielded a reconstruction map at 3.65 Å.

The procedures for DHEAS-bound ABCC3 were performed on the cryoSPARC 3.2 (Punjani *et al*, 2017). A total of 560,123 particles

from 1,118 micrographs and 1,323,642 particles from 2,522 micrographs were automatically picked out and subjected to 2D classification (Appendix Fig S12A–E). After several rounds of 2D classification, the better particles were selected at an unbinned pixel size of 1.07 Å for 3D classification. Totally, 240,291 particles reconstruct a 3.52 Å map by non-uniform refinement and local refinement.

All resolutions of the cryo-EM maps were estimated using the gold-standard Fourier shell correlation 0.143 criterion (Kucukelbir *et al*, 2014).

Model building and refinement

The apo-form model of ABCC3 was generated by the SWISS-MODEL server (Waterhouse *et al*, 2018), using the cryo-EM structure of *Bos taurus* ABCC1 (PDB code 5uj9) as the reference model and corrected based on the structure of human ABCC3 predicted by alphafold2. The rebuilt model was refined using real-space refinement in PHENIX (Adams *et al*, 2010) with secondary structure and geometry restraints. The ABC core part can be built well according to the template model, but the electron density of TMD0 does not match it obviously. For the TMD0 region, of these three maps, the highest quality of electron density in the DHEAS-bound map TMD0 region allowed unambiguous assignment of residues. Therefore, the TMD0 model of DHEAS-bound structure was manually rebuilt in COOT (Emsley & Cowtan, 2004), refined using real-space refinement in PHENIX, and then fitted into the TMD0 electron density of apo-form and $E_2$17βG-bound maps by rigid-body fitting. In the structure of $E_2$17βG-bound ABCC3, two extra asymmetric densities between TMD1 and TMD2 can be observed, each of which was fitted by an $E_2$17βG molecule (Appendix Fig S11E). All parts except TMD0 were manually fitted into map with the structure predicted by alphafold2 as a model, adjusted according to the electron density and automatically refined in PHENIX (Adams *et al*, 2010). For the DHEAS-bound ABCC3, at the same position of TMD1 and TMD2, we also observed two additional densities fitted by two DHEAS molecules (Appendix Fig S12E). The main methods of model building are similar to the above. The final model contains residues Phe32-Ala268, Lys296-Cys850, Ala949-Met1520, and two DHEAS molecules. The programs of UCSF Chimera (Pettersen *et al*, 2004), ChimeraX (Pettersen *et al*, 2021), and PyMOL (The PyMOL Molecular Graphics System, Version 2.5.2 Copyright (C) Schrödinger, LLC.) were used for preparing the structural figures. Protein sequences were aligned using Multalin (http://multalin.toulouse.inra.fr/multalin/), and the sequence-alignment figures were generated by ESPript 3 server (https://espript.ibcp.fr/).

Data availability

All relevant data are available from the authors and/or included in the manuscript or Supplementary Information. Atomic coordinates and EM density maps of the human ABCC3 (PDB: 8HVH; EMDB: EMD-35043), ABCC3 complexed with $E_2$17βG (PDB: 8HW2; EMDB: EMD-35049) and with DHEAS (PDB: 8HW4; EMDB: EMD-35050) in this paper have been deposited in the Protein Data Bank and the Electron Microscopy Data Bank, respectively.

Expanded View for this article is available online.

Acknowledgments

We thank Dr. Yong-xiang Gao at the Center for Integrative Imaging, University of Science and Technology of China during cryo-EM image acquisition. We thank Xiao-jun Huang and Xu-jing Li at the Center for Biological Imaging at the Institute of Biophysics (IBP), Chinese Academy of Sciences for technical support on cryo-EM data collection. This work was supported by the Strategic Priority Research Program of the Chinese Academy of Sciences (XDB37020202), the Ministry of Science and Technology of China (2019YFA0508500), China Postdoctoral Science Foundation (2022M723050) and Research Funds of Center for Advanced Interdisciplinary Science and Biomedicine of IHM (QYZD20220001).

Author contributions

Jie Wang: Conceptualization; data curation; software; formal analysis; validation; investigation; visualization; writing – original draft. **Xu Li:** Conceptualization; formal analysis; writing – original draft. **Fang-Fang Wang:** Data curation; formal analysis. **Meng-Ting Cheng:** Conceptualization; formal analysis; validation. **Yao-Xu Mao:** Conceptualization; methodology. **Shu-Cheng Fang:** Validation; methodology. **Liang Wang:** Software; formal analysis; methodology. **Cong-Zhao Zhou:** Conceptualization; resources; supervision; visualization; writing – review and editing. **Wen-Tao Hou:** Conceptualization; formal analysis; supervision; methodology; writing – review and editing. **Yuxing Chen:** Conceptualization; resources; supervision; funding acquisition; writing – review and editing.

Disclosure and competing interests statement

The authors declare that they have no conflict of interest.

References

Adams PD, Afonine PV, Bunkóczi G, Chen VB, Davis IW, Echols N, Headd JJ, Hung LW, Kapral GJ, Grosse-Kunstleve RW *et al* (2010) PHENIX: a comprehensive python-based system for macromolecular structure solution. *Acta Crystallogr D Biol Crystallogr* 66: 213 – 221

Aller SG, Yu J, Ward A, Weng Y, Chittaboina S, Zhuo R, Harrell PM, Trinh YT, Zhang Q, Urbatsch IL *et al* (2009) Structure of P-glycoprotein reveals a molecular basis for poly-specific drug binding. *Science* 323: 1718 – 1722

Bakos E, Evers R, Szakács G, Tusnády GE, Welker E, Szabó K, de Haas M, van Deemter L, Borst P, Váradi A *et al* (1998) Functional multidrug resistance protein (MRP1) lacking the N-terminal transmembrane domain. *J Biol Chem* 273: 32167 – 32175

Bickers SC, Benlekbir S, Rubinstein JL, Kanelis V (2021) Structure of Ycf1p reveals the transmembrane domain TMD0 and the regulatory region of ABCC transporters. *Proc Natl Acad Sci USA* 118: e2025853118

Borst P, de Wolf C, van de Wetering K (2007) Multidrug resistance-associated proteins 3, 4, and 5. *Pflügers Arch* 453: 661 – 673

Chan KW, Zhang H, Logothetis DE (2003) N-terminal transmembrane domain of the SUR controls trafficking and gating of Kir6 channel subunits. *EMBO J* 22: 3833 – 3843

Dash RP, Jayachandra Babu R, Srinivas NR (2017) Therapeutic potential and utility of Elacridar with respect to P-glycoprotein inhibition: an insight from the published in vitro, preclinical and clinical studies. *Eur J Drug Metab Pharmacokinet* 42: 915 – 933

Demirel O, Bangert I, Tampé R, Abele R (2010) Tuning the cellular trafficking of the lysosomal peptide transporter TAPL by its N-terminal domain. *Traffic* 11: 383 – 393

Emsley P, Cowtan K (2004) Coot: model-building tools for molecular graphics. *Acta Crystallogr D Biol Crystallogr* 60: 2126 – 2132

Fiedorczuk K, Chen J (2022a) Mechanism of CFTR correction by type I folding correctors. *Cell* 185: 158 – 168.e11

Fiedorczuk K, Chen J (2022b) Molecular structures reveal synergistic rescue of Δ508 CFTR by Trikafta modulators. *Science* 378: 284 – 290

Gabzdyl EM, Schlaeger JM (2015) Intrahepatic cholestasis of pregnancy: a critical clinical review. *J Perinat Neonatal Nurs* 29: 41 – 50

Ghanem CI, Manautou JE (2019) Modulation of hepatic MRP3/ABCC3 by Xenobiotics and pathophysiological conditions: role in drug pharmacokinetics. *Curr Med Chem* 26: 1185 – 1223

Gottesman MM, Fojo T, Bates SE (2002) Multidrug resistance in cancer: role of ATP-dependent transporters. *Nat Rev Cancer* 2: 48 – 58

Grant DM (1991) Detoxification pathways in the liver. *J Inherit Metab Dis* 14: 421 – 430

Gu X, Manautou JE (2010) Regulation of hepatic ABCC transporters by xenobiotics and in disease states. *Drug Metab Rev* 42: 482 – 538

Järvinen E, Kidron H, Finel M (2020) Human efflux transport of testosterone, epitestosterone and other androgen glucuronides. *J Steroid Biochem Mol Biol* 197: 105518

Jedlitschky G, Leier I, Buchholz U, Hummel-Eisenbeiss J, Burchell B, Keppler D (1997) ATP-dependent transport of bilirubin glucuronides by the multidrug resistance protein MRP1 and its hepatocyte canalicular isoform MRP2. *Biochem J* 327: 305 – 310

Johnson ZL, Chen J (2017) Structural basis of substrate recognition by the multidrug resistance protein MRP1. *Cell* 168: 1075 – 1085.e9

Johnson ZL, Chen J (2018) ATP binding enables substrate release from multidrug resistance protein 1. *Cell* 172: 81 – 89.e10

Keppler D (2014) The roles of MRP2, MRP3, OATP1B1, and OATP1B3 in conjugated hyperbilirubinemia. *Drug Metab Dispos* 42: 561 – 565

Keppler D, König J (2000) Hepatic secretion of conjugated drugs and endogenous substances. *Semin Liver Dis* 20: 265 – 272

Khandelwal NK, Millan CR, Zangari SI, Avila S, Williams D, Thaker TM, Tomasiak TM (2022) The structural basis for regulation of the glutathione transporter Ycf1 by regulatory domain phosphorylation. *Nat Commun* 13: 1278

Koch J, Guntrum R, Heintke S, Kyritsis C, Tampé R (2004) Functional dissection of the transmembrane domains of the transporter associated with antigen processing (TAP). *J Biol Chem* 279: 10142 – 10147

König J, Rost D, Cui Y, Keppler D (1999) Characterization of the human multidrug resistance protein isoform MRP3 localized to the basolateral hepatocyte membrane. *Hepatology* 29: 1156 – 1163

Kool M, de Haas M, Scheffer GL, Scheper RJ, van Eijk MJ, Juijn JA, Baas F, Borst P (1997) Analysis of expression of cMOAT (MRP2), MRP3, MRP4, and MRP5, homologues of the multidrug resistance-associated protein gene (MRP1), in human cancer cell lines. *Cancer Res* 57: 3537 – 3547

Kool M, van der Linden M, de Haas M, Scheffer GL, de Vree JM, Smith AJ, Jansen G, Peters GJ, Ponne N, Scheper RJ *et al* (1999) MRP3, an organic anion transporter able to transport anti-cancer drugs. *Proc Natl Acad Sci USA* 96: 6914 – 6919

Kucukelbir A, Sigworth FJ, Tagare HD (2014) Quantifying the local resolution of cryo-EM density maps. *Nat Methods* 11: 63 – 65

Kulsharova G, Kurmangaliyeva A (2021) Liver microphysiological platforms for drug metabolism applications. *Cell Prolif* 54: e13099

Lammert F, Marschall HU, Glantz A, Matern S (2000) Intrahepatic cholestasis of pregnancy: molecular pathogenesis, diagnosis and management. *J Hepatol* 33: 1012 – 1021

Lee YM, Cui Y, König J, Risch A, Jäger B, Drings P, Bartsch H, Keppler D, Nies AT (2004) Identification and functional characterization of the natural variant MRP3-Arg1297His of human multidrug resistance protein 3 (MRP3/ABCC3). *Pharmacogenetics* 14: 213 – 223

Lee KPK, Chen J, MacKinnon R (2017) Molecular structure of human KATP in complex with ATP and ADP. *Elife* 6: e32481

Levring J, Terry DS, Kilic Z, Fitzgerald G, Blanchard S, Chen J (2023) CFTR function, pathology and pharmacology at single-molecule resolution. *Nature* 616: 606 – 614

Li CY, Basit A, Gupta A, Gáborik Z, Kis E, Prasad B (2019) Major glucuronide metabolites of testosterone are primarily transported by MRP2 and MRP3 in human liver, intestine and kidney. *J Steroid Biochem Mol Biol* 191: 105350

Liu F, Zhang Z, Csanády L, Gadsby DC, Chen J (2017) Molecular structure of the human CFTR ion channel. *Cell* 169: 85 – 95.e8

Maltbaek JH, Cambier S, Snyder JM, Stetson DB (2022) ABCC1 transporter exports the immunostimulatory cyclic dinucleotide cGAMP. *Immunity* 55: 1799 – 1812.e4

Martin GM, Sung MW, Yang Z, Innes LM, Kandasamy B, David LL, Yoshioka C, Shyng SL (2019) Mechanism of pharmacochaperoning in a mammalian K (ATP) channel revealed by cryo-EM. *Elife* 8: e46417

Middleton PG, Mall MA, Dřevínek P, Lands LC, McKone EF, Polineni D, Ramsey BW, Taylor-Cousar JL, Tullis E, Vermeulen F *et al* (2019) Elexacaftor-Tezacaftor-Ivacaftor for cystic fibrosis with a single Phe508del allele. *N Engl J Med* 381: 1809 – 1819

Morikawa A, Goto Y, Suzuki H, Hirohashi T, Sugiyama Y (2000) Biliary excretion of 17beta-estradiol 17beta-D-glucuronide is predominantly mediated by cMOAT/MRP2. *Pharm Res* 17: 546 – 552

Ovadia C, Williamson C (2016) Intrahepatic cholestasis of pregnancy: recent advances. *Clin Dermatol* 34: 327 – 334

Pettersen EF, Goddard TD, Huang CC, Couch GS, Greenblatt DM, Meng EC, Ferrin TE (2004) UCSF Chimera?A visualization system for exploratory research and analysis. *J Comput Chem* 25: 1605 – 1612

Pettersen EF, Goddard TD, Huang CC, Meng EC, Couch GS, Croll TI, Morris JH, Ferrin TE (2021) UCSF ChimeraX: structure visualization for researchers, educators, and developers. *Protein Sci* 30: 70 – 82

Punjani A, Rubinstein JL, Fleet DJ, Brubaker MA (2017) cryoSPARC: algorithms for rapid unsupervised cryo-EM structure determination. *Nat Methods* 14: 290 – 296

Rao ZZ, Zhang XW, Ding YL, Yang MY (2017) miR-148a-mediated estrogen-induced cholestasis in intrahepatic cholestasis of pregnancy: role of PXR/MRP3. *PloS One* 12: e0178702

Rees DC, Johnson E, Lewinson O (2009) ABC transporters: the power to change. *Nat Rev Mol Cell Biol* 10: 218 – 227

Ritchie TK, Grinkova YV, Bayburt TH, Denisov IG, Zolnerciks JK, Atkins WM, Sligar SG (2009) Chapter 11 – reconstitution of membrane proteins in phospholipid bilayer nanodiscs. *Methods Enzymol* 464: 211 – 231

Rutkowski K, Sowa P, Rutkowska-Talipska J, Kuryliszyn-Moskal A, Rutkowski R (2014) Dehydroepiandrosterone (DHEA): hypes and hopes. *Drugs* 74: 1195 – 1207

Scheffer GL, Kool M, de Haas M, de Vree JM, Pijnenborg AC, Bosman DK, Elferink RP, van der Valk P, Borst P, Scheper RJ (2002) Tissue distribution and induction of human multidrug resistant protein 3. *Lab Invest* 82: 193 – 201

Seelig A, Blatter XL, Wohnsland F (2000) Substrate recognition by P-glycoprotein and the multidrug resistance-associated protein MRP1: a comparison. *Int J Clin Pharmacol Ther* 38: 111 – 121

Sharom FJ (2011) The P-glycoprotein multidrug transporter. *Essays Biochem* 50: 161 – 178

Stieger B, Fattinger K, Madon J, Kullak-Ublick GA, Meier PJ (2000) Drug- and estrogen-induced cholestasis through inhibition of the hepatocellular bile salt export pump (Bsep) of rat liver. *Gastroenterology* 118: 422 – 430

Stillwell W (2016) Chapter 20 – bioactive lipids. In *An introduction to biological membranes*, Stillwell W (ed), 2nd edn, pp 453–478. Amsterdam, The Netherlands: Elsevier

Sung MW, Yang Z, Driggers CM, Patton BL, Mostofian B, Russo JD, Zuckerman DM, Shyng SL (2021) Vascular K(ATP) channel structural dynamics reveal regulatory mechanism by Mg-nucleotides. *Proc Natl Acad Sci USA* 118: e2109441118

Thomas C, Tampé R (2020) Structural and mechanistic principles of ABC transporters. *Annu Rev Biochem* 89: 605–636

Tukey RH, Strassburg CP (2000) Human UDP-glucuronosyltransferases: metabolism, expression, and disease. *Annu Rev Pharmacol Toxicol* 40: 581–616

Vardakou M, Salmon M, Faraldos JA, O'Maille PE (2014) Comparative analysis and validation of the malachite green assay for the high throughput biochemical characterization of terpene synthases. *MethodsX* 1: 187–196

Wang L, Johnson ZL, Wasserman MR, Levring J, Chen J, Liu S (2020) Characterization of the kinetic cycle of an ABC transporter by single-molecule and cryo-EM analyses. *Elife* 9: e56451

Waterhouse A, Bertoni M, Bienert S, Studer G, Tauriello G, Gumienny R, Heer FT, de Beer TAP, Rempfer C, Bordoli L *et al* (2018) SWISS-MODEL: homology modelling of protein structures and complexes. *Nucleic Acids Res* 46: W296–w303

Westlake CJ, Qian YM, Gao M, Vasa M, Cole SP, Deeley RG (2003) Identification of the structural and functional boundaries of the multidrug resistance protein 1 cytoplasmic loop 3. *Biochemistry* 42: 14099–14113

Wilson BR, Haverkamp AD (1979) Cholestatic jaundice of pregnancy: new perspectives. *Obstet Gynecol* 54: 650–652

Wu JX, Ding D, Wang M, Kang Y, Zeng X, Chen L (2018) Ligand binding and conformational changes of SUR1 subunit in pancreatic ATP-sensitive potassium channels. *Protein Cell* 9: 553–567

Yang G, Ge S, Singh R, Basu S, Shatzer K, Zen M, Liu J, Tu Y, Zhang C, Wei J *et al* (2017) Glucuronidation: driving factors and their impact on glucuronide disposition. *Drug Metab Rev* 49: 105–138

Zehnpfennig B, Urbatsch IL, Galla HJ (2009) Functional reconstitution of human ABCC3 into proteoliposomes reveals a transport mechanism with positive cooperativity. *Biochemistry* 48: 4423–4430

Zeng H, Bain LJ, Belinsky MG, Kruh GD (1999) Expression of multidrug resistance protein-3 (multispecific organic anion transporter-D) in human embryonic kidney 293 cells confers resistance to anticancer agents. *Cancer Res* 59: 5964–5967

Zeng H, Liu G, Rea PA, Kruh GD (2000) Transport of amphipathic anions by human multidrug resistance protein 3. *Cancer Res* 60: 4779–4784

Zu Y, Yang J, Zhang C, Liu D (2021) The pathological mechanisms of estrogen-induced cholestasis: current perspectives. *Front Pharmacol* 12: 761255